Supplementary Material: Simulating terahertz field-induced ferroelectricity in quantum paraelectric $SrTiO_3$

Dongbin Shin,[1,2,*] Simone Latini,[1] Christian Schäfer,[1] Shunsuke A. Sato,[3,1] Edoardo Baldini,[4] Umberto De Giovannini,[1,5] Hannes Hübener,[1] and Angel Rubio[1,5,6,†]

[1] *Max Planck Institute for the Structure and Dynamics of Matter and Center for Free Electron Laser Science, 22761 Hamburg, Germany*

[2] *Department of Physics and Photon Science, Gwangju Institute of Science and Technology (GIST), Gwangju 61005, Republic of Korea*

[3] *Center for Computational Sciences, University of Tsukuba, Tsukuba 305-8577, Japan*

[4] *Department of Physics, The University of Texas at Austin, 78712 Austin, Texas Massachusetts, USA*

[5] *Nano-Bio Spectroscopy Group, Departamento de Fisica de Materiales, Universidad del País Vasco UPV/EHU- 20018 San Sebastián, Spain*

[6] *Center for Computational Quantum Physics (CCQ), The Flatiron Institute, 162 Fifth avenue, New York NY 10010.*

FITTING COEFFICIENTS OF POTENTIAL ENERGY SURFACE

Our study solved the 2D Schrödinger equation with a 2D FES-lattice potential energy surface. To evaluate this 2D potential energy surface, we calculate DFT total energy $E^{2D}_{DFT}[Q_{\rm f}, Q_{\rm c}]$ by distorting the atomic geometry along the FES mode, parameterized by $Q_{\rm f}$ and the c-axis, parameterized by $Q_{\rm c}$. The variable $Q_{\rm f}$ is defined as follows: $Q_f = x(U^{\rm FES}_{\rm Ti,z} - U^{\rm FES}_{\rm O,z}) = xd$, which is the atomic displacement difference between Ti and O atoms along the z-direction in the normalized eigenvector of FES mode U parameterized by x. The normalized eigenvector U is obtained from the optimized geometry difference between ferroelectric (dE$[Q_f \neq 0]/dQ_f = 0$ and $Q_c = 0$) and paraeletric $SrTiO_3$ ($Q_f = 0$) in the tetragonal unit cell. The $Q_{\rm c}$ is defined as uniaxial lattice variation along the FES mode direction from the strain free lattice $Q_{\rm c} = 0$. The fitting coefficients of the potential energy surface ($V^{2D}[Q_{\rm f}, Q_{\rm c}] = E^{2D}_{DFT}[Q_{\rm f}, Q_{\rm c}] - E^{2D}_{DFT}[0, 0]$) are evaluated up to the 24-th order for $Q_{\rm f}$ and 10-th order for $Q_{\rm c}$ as follows:

$$\hat{V}^{\rm 2D}[Q_{\rm f}, Q_{\rm c}] = \sum_{i=1}^{12} k_{f,i}\hat{Q}_f^{2i} + \sum_{j=2}^{10} k_{c,j}\hat{Q}_c^{j} + \sum_{i=1}^{12}\sum_{j=1}^{10} k_{fc,i,j}\hat{Q}_f^{2i}\hat{Q}_c^{j} \tag{S1}$$

This high-order fitting coefficient reproduces an almost identical potential energy surface compared with the potential energy surface obtained by DFT calculation. The evaluated fitting coefficients are summarized in Tables S1 and S2.

In addition, we also considered the effect of AFD mode through the classical treatment. The modified potential energy surface of FES mode and c-axis by AFD mode at given time t is given as follows: $\hat{V}^{f,c,a} = \sum_{i=1}^{10}\sum_{j=1}^{12} k_{af,i,j}Q_a^i\hat{Q}_f^{2j} + \sum_{i=1}^{10}\sum_{j=1}^{10} k_{ac,i,j}Q_a^i\hat{Q}_c^{\ j}$ The evaluated fitting coefficients are summarized in Tables S3, S4, S5, and S6.

SOLVING TIME-DEPENDENT SCHRÖDINGER-LANGEVIN EQUATION

To investigate the THz field-induced ferroeletricity in $SrTiO_3$, we solve the time-dependent lattice Schrödinger-Langevin equation with dissipation effect as follows [1, 2]:

$$\frac{d}{dt}\psi = \hat{H}_{\rm 3D}\psi + \gamma(\hat{S} - <\hat{S}>)\psi. \tag{S2}$$

The 3D lattice Hamiltonian ($\hat{H}_{3D}$) consists of ferroeletric soft mode ($\hat{Q}_f$), lattice ($\hat{Q}_c$) and given AFD mode (Q_a) at t. To include the dissipation effect, the phase of wavefunction ($\hat{S}[Q_f, Q_c, t] = arg[\psi(Q_f, Q_c, t)]$) is evaluated with dissipation ratio γ [1, 2]. To construct the Hamiltonian, the numerical grid basis set is considered 200×200 for the -0.5 Å $\leq Q_f \leq 0.5$ Å and -0.2 Å $\leq Q_c \leq 0.4$ Å, and its convergence is checked up to 500×500. The application of the kinetic term is done using central finite difference for a uniform grid spacing up to the 8-th order as follows:

$$\begin{aligned} f''(x_0) =& [-\frac{1}{560}f(x_{-4}) + \frac{8}{315}f(x_{-3}) - \frac{1}{5}f(x_{-2}) + \frac{8}{5}f(x_{-1}) \\ & - \frac{205}{72}f(x_0) + \frac{8}{5}f(x_1) - \frac{1}{5}f(x_2) + \frac{8}{315}f(x_3) - \frac{1}{560}f(x_4)]/h_x^2 \end{aligned} \tag{S3}$$

We employed the time-evolution operator with Taylor expansion up to 4-th order as follows:

$$\hat{U}(t + dt; t) = [1 + \sum_{1}^{4}(\frac{-idt}{2\hbar})^n \frac{\hat{H}^n}{n!}][1 + \sum_{1}^{4}(\frac{-idt}{2\hbar})^n \frac{\hat{H}^n}{n!}] \tag{S4}$$

HEAT DISSIPATION THROUGH THE OHMIC BATH IN THE SCHRÖDINGER-LANGEVIN EQUATION

To investigate the non-equilibrium dynamics with dissipation, we solve the Schrödinger-Langevin equation as follows: $\frac{d}{dt}\psi = \hat{H}\psi + \gamma(\hat{S} - < \hat{S} >)\psi$, when γ and $\hat{S}[Q_f, Q_c] = arg[\psi(Q_f, Q_c, t)]$ are the dissipation rate and the phase of the wavefunction respectively. Former studies investigate real-time dynamics of the 1-dimension and 2-dimension wavefunction with heat dissipation to describe the quantum vibrations of molecules or phonon [1, 2]. For example, the Schrodinger-Langevin equation reveals real-time dynamics of quantum wavefunction consisting of C-I and C-H_3 vibrations of methyl iodide, and this method provides consistent results with exact solutions [2]. It is also used to investigate the time-propagation of a wavefunction in double-well potential using Schrödinger-Langevin equation [1]. These works indicate that the Schrodinger-Langevin equation can lead to reliable real-time quantum dynamics with fractional dissipation.

The dissipation path through harmonic oscillators has been considered for the open quan-

tum systems [3–5]. In previous studies, the Ohmic environment is employed to describe the dissipation through harmonic oscillators with and without nonlinear coupling [3–5]. In our study, we assume that the energy of the FES mode excited by the THz field pulse is mainly dissipated into the other phonon modes. Considering that bulk $SrTiO_3$ is a 2 eV bandgap insulator, the dissipation channel through electron-phonon scattering can be comparably negligible. Here, we investigate the decaying ratio of FES mode through the AIMD simulation in a $2\times2\times2$ supercell. With initially displaced atomic geometry along the FES mode, we then evaluated the time profile of the absolute value of FES mode under the NPE-ensemble as shown in Fig. S1(a). Because NPE-ensemble sustains the number of particles, constant pressure, and constant energy, it makes possible to investigate the dissipation of FES mode through the phonon-phonon scattering. We found that the initially excited FES mode dissipates into other modes such as the c-axis, AFD, and a-axis (see Fig. S9). By fitting an exponential decay curve ($a_0e^{-\gamma t}$), the fitting parameters a_0 = 14.8 mÅ and γ = 1.5 THz are obtained. We evaluate the decaying ratio (γ) in a wide range of initial displacement of FES mode, as shown in Fig. S1(b). Our results indicate that the decaying ratio is strongly dependent on the initial displacement of the FES mode. Because the larger initial displacement of FES mode contains much higher energy compared to the heat bath in the $2 \times 2 \times 2$ supercell, which is the computational limit of our dynamics (117 degrees of freedom), hence the energy of FES mode cannot yet be efficiently dissipated. To check the contribution of the AFD and c-axis motion on the dissipation, we also evaluate the decaying ratio with constrained AIMD simulation. The decaying ratio is evaluated by fixing the c-axis lattice and movements of oxygen atoms along with the AFD mode, as shown in Fig. S1(b). We found that AIMD without the AFD and c-axis dynamics does not provide different decaying behavior when compared to the full dynamics. This result indicates that the excited FES mode dissipates into all phonon modes rather than specific phonon modes as AFD and c-axis in $SrTiO_3$. To estimate the appropriate dissipation ratio in our simulation, we evaluate the average absolute value of the excited FES mode by THz field pulse without dissipation, as shown in Fig. S1(c). Even though the time propagation with a short period ($t < 12$ ps) does not provide a clear converged trend, the $|Q_f|^{avg} \sim 20$ mÅ is evaluated in a wide range of field strength with the time-propagation. With this estimation, we employ a damping rate of $\gamma = 1.2$ THz and report the dissipation ratio's dependency on the THz field-induced ferroelectricity in our updated manuscript. Notably, a previous study reported the dissipation

ratio $\gamma = 0.9$ THz evaluated from the lifetime of FES mode observed in spectroscopy to demonstrate the THz-field pulse-induced nonlinear phonon interaction in $SrTiO_3$ [6].

We also check the effect of heat baths on the dissipation of FES mode through the AIMD simulation. As shown in Fig. S1(d), the dynamics of FES mode are evaluated by the AIMD simulation with NPT-ensemble and the same initial condition ($Q_f(t = 0) = 20$ mÅ) as the previous case. Because the thermostat constrains the ionic motion at a given temperature, the decay rate of FES mode with the thermostat at 10 K is significantly decreased ($\sim$ 0.085 THz). Considering the decay process by the heat bath (γ_{thermo}) is comparably slow, the contribution of phonon-phonon scattering on the decay of the FES mode is dominant (γ_{ph}). This result indicates that our estimation of the decay rate of FES mode with NPE-ensemble is appropriate.

In our updated results, the THz-field induced ferroelectricity is achieved in a field strength range of 200 $\sim$ 450 kV/cm as shown in Fig 1(e) consistent with experimental results, but unlike the experiment the decay back to the quantum paraelectric phase on a few ps time-scale is not captured. The inconsistency brought by this non-decaying behavior might originate from the lack of finite-temperature heat bath, and the simplified description of the phonon-phonon scattering processes in our model. Nevertheless our calculations serve the purpose of unravelling the microscopic mechanism behind THz field-induced ferroelectricity in $SrTiO_3$.

MODE EFFECTIVE CHARGE, NORMALIZED EIGENVECTOR OF FES MODE, AND EFFECTIVE FIELD STRENGTH IN MEDIUM

We evaluated the Born effective charge for each atom with density functional perturbation theory and obtained Z_{Sr}=2.58 e, Z_{Ti}=7.30 e, $Z_{\mathrm{O,z}}$=-5.74 e, and $Z_{\mathrm{O,xy}}$=-2.08 e. which are consistent with previous calculations [7, 8]. We defined the mode effective charge for the ferroeletric soft mode as follows: $Z_f = \sum_a Z_a(\frac{U^{\mathrm{FES}}_{\mathrm{a,z}}}{U^{\mathrm{FES}}_{\mathrm{Ti,z}} - U^{\mathrm{FES}}_{\mathrm{O,z}}}) = 37.2$ e for the tetragonal unit cell. The normalized eigenvector and details of tetragonal $SrTiO_3$ are summarized in Table S7.

We evaluate the mode effective charge from the modified potential energy surface by applying finite E-field on the bulk $SrTiO_3$. From the modern theory of polarization, the minimized total energy of density of the state is achieved with finite E-field in the periodic boundary condition [9]. As shown in Fig. S2(a), the potential energy surface of

FES mode is modified depending on E-field strength. The mode effective charge is evaluated from the first derivative of energy potential energy (U) difference as follows: $Z = \frac{1}{eE_{field}}\frac{\delta}{\delta Q_f}(U_{DFT}[Q_f, E_{field}] - U_{DFT}[Q_f, 0])$. We found that the mode effective charge is not significantly dependent on the field strength, but it is almost constant in a wide range of field strength ($Z_{tetra} = 37\ e$) as shown in Fig. S2(b).

We also consider the effective field strength (E_{eff}) in the $SrTiO_3$ to compare the applied field strength in experiment. The effective field strength in medium and incident field have a relation as follows: $E_{\text{eff}} = \frac{2}{1+\sqrt{\epsilon(\omega)}}E_{\text{ext}}$, when $\epsilon(\omega)$ is dielectric function at given frequency [10]. The dielectric function of $SrTiO_3$ at low frequency is approximately $\epsilon \sim 6$ [11, 12]. With these results in the former studies, we evaluate the effective E-field ($E_{\text{eff}}(t) = 0.58E_{\text{ext}}(t)$) in the medium from the E_{ext} external field strength.

CONVERTING THE HAMILTONIAN INTO NORMAL MODE COORDINATE

In our simulation, we perform the time propagation with the following Hamiltonian:

$$\hat{H}_{\text{2D}}[Q_f, Q_c, t] = \frac{\hat{P}_f^2}{2M_f} + \frac{\hat{P}_c^2}{2M_c} + \hat{V}_{\text{2D}}^{\text{FES,c}} + E_{ext}(t)Z_f\hat{Q}_f, \tag{S4}$$

where the mass for the FES mode is defined as $M_f = \sum_a M_a(\frac{U_{a,z}^{\text{FES}}}{U_{\text{Ti,z}}^{\text{FES}} - U_{\text{O,z}}^{\text{FES}}})^2$ and the mass for lattice is defined as $M_c = \sum_a M_a$ [13]. The Schrödinger equation is written in Å unit and expressed in terms of Q_f, Q_c, $P_f = M_f\frac{dQ_f}{dt}$ and $P_c = M_c\frac{dQ_c}{dt}$. In previous studies on light-matter interaction [14–19], the nonlinear phonon interaction driven by external fields has been investigated with a classical equation of motion as follows; $\ddot{Q} + \frac{dV}{dQ} + \gamma\dot{Q} = ZE$, when Q, V, Z, and E are normal mode coordinates, potential surface, mode effective charge, and external field, respectively. In that case, Q is defined in the unit of length $\times\sqrt{\text{Mass}}$ for this equation of motion. Even though we used Q in the unit of length for the conventional expression in Schödinger equation, the Q can be easily converted to the normal mode coordinates in the unit of length $\times\sqrt{\text{Mass}}$ (Q_{fm}) as follows; $Q_{fm} = \sqrt{M_{fm}}Q_f/d$, when $d = U_{\text{Ti,z}}^{\text{FES}} - U_{\text{O,z}}^{\text{FES}} = 0.514$ and $M_{fm} = d^2M_f = 28.11$ amu. The momentum $P_f = M_f\frac{dQ_f}{dt}$ in our manuscript can be also converted into the momentum in normal mode coordinates

as follows; $P_{fm} = \frac{dQ_{fm}}{dt} = \frac{\sqrt{M_{fm}}}{dM_f} P_f$. From the simple Hamiltonian ($P_f^2/2M_f + kQ_f^2$) in the Q_f coordinate, the Hamiltonian in normal mode coordinate becomes $P_{fm}^2/2 + \frac{kd^2}{M_{fm}} Q_{fm}^2$. In addition, the mode effective charge Z_f is also converted to $Z_{fm} = Z_f d/\sqrt{M_{fm}}$. In the cubic cell, the mode effective charge in normal coordinate is $Z_{fm,cubic} = Z_{fm}/4 = 0.91\ e\ amu^{-1/2}$ With these conversions, the equation (S4) becomes as follows;

$$\hat{H}_{\mathrm{2D}}[Q_{fm}, Q_{cm}, t] = \frac{\hat{P}_{fm}^2}{2} + \frac{\hat{P}_{cm}^2}{2} + \hat{\tilde{V}}_{\mathrm{2D}}^{\mathrm{FES,c}} + E_{ext}(t) Z_{fm} \hat{Q}_{fm}, \tag{S5}$$

$$\text{when } \hat{\tilde{V}}_{\mathrm{2D}}^{\mathrm{FES,c}} = \sum_{\mathrm{i}=1}^{12} \frac{\mathrm{k_{f,i}}}{\mathrm{M_{fm}}^{\mathrm{i}}} \hat{\mathrm{Q}}_{\mathrm{fm}}^{\mathrm{2i}} + \sum_{\mathrm{j}=2}^{10} \frac{\mathrm{k_{c,j}}}{\mathrm{M_{cm}^{j}}} \hat{\mathrm{Q}}_{\mathrm{cm}}^{\mathrm{j}} + \sum_{\mathrm{i}=1}^{12} \sum_{\mathrm{j}=1}^{10} \frac{\mathrm{k_{fc,i,j}}}{\mathrm{M_{fm}}^{\mathrm{i}} \mathrm{M_{cm}}^{\mathrm{j/2}}} \hat{\mathrm{Q}}_{\mathrm{fm}}^{\mathrm{2i}} \hat{\mathrm{Q}}_{\mathrm{cm}}^{\mathrm{j}}. \tag{S6}$$

FERROELECTRIC STATE FROM THE EXCITATION BETWEEN GROUND AND FIRST EXCITED STATES IN THE QUANTUM PARAELECTRIC PHASE

The quantum paraelectric phase in $SrTiO_3$ has the non-degenerated ground (ψ_0) and first excited (ψ_1) states, in which energy difference corresponds to the frequency of the ferroelectric soft mode ($\omega = \epsilon_1 - \epsilon_0 = 0.5$ THz) [13]. As shown in Figs. S3(a) and S3(b), the excitation between ground and first excited states can provide the ferroelectric states. As shown in Figs. S3(c) and S3(d), the linear combination of ground and first excited states indicates the ferroelectric lattice wavefunction, in which lattice density locates the one of double-well potential. Our study found that a single cycle THz field pulse leads to the ferroelectric state.

SECOND-HARMONIC GENERATION SIGNAL WITH DISTORTED GEOMETRIES

To evaluate the second harmonic generation signal from the time-profile of ferroelectric soft mode, we computed second harmonic generation signal in the $\sqrt{2} \times \sqrt{2} \times 2$ tetragonal geometry $SrTiO_3$ using time-dependent density functional theory calculation [20]. We distorted the atomic geometry toward the ferroelectric soft mode direction (Q_f) from its optimized paraelectric tetragonal geometry. With this fixed geometry, we apply the 1.55 eV prove pulse with 40 fs duration [21] and evaluated the second harmonic generation response

in the inset of Fig. 2(f) in the main text. Considering the time scale of THz field-induced lattice dynamics ($\sim$ 10 ps), the motion of lattice is negligible during this electronic response. We evaluate fitting parameters of the second harmonic generation signal concerning atomic distortion along the Q_f as follows:

$$SHG(Q_f) = \sum_{i}^{3} c_i |Q_f|^i. \tag{S6}$$

Table S8 shows summarized coefficients. Notably, the second harmonic generation signal is an even function for Q_f. We evaluated the second harmonic generation signal of THz-induced lattice wavefunction with this relation, as shown in Fig. 2(e) in the main text.

FREQUENCY OF FES MODE FROM THE OPTICAL SPECTRUM

Here we also provide the eigenvalue of gamma phonon modes in cubic $SrTiO_3$ evaluated from density functional perturbation theory (DFPT) in the wide range of frequency up to 16 THz $\sim 500cm^{-1}$ as shown in Fig S4. Through the DFPT calculation, we found the triply-degenerated phonon modes with positive frequency except for the FES modes in the cubic unit cell. The Schrödinger equation evaluates the non-negative phonon frequency of FES mode (0.48 THz), while the DFPT calculation gives a negative phonon frequency of FES mode [13]. Similar to the former experiment report [6], we found two IR-active TO modes at 4 THz and 15 THz and a silent TO mode at 6.5 THz. Compared with the spectrum of THz-field pulse, the only resonant IR-active mode is FES mode, as shown in Fig. S4(b). Even though the single-cycle pulse has broadened the spectrum in the frequency domain, the FES mode is the only mode that resonates with this THz-field pulse. We also checked the phonon density of the state in the tetragonal $SrTiO_3$ as shown in Fig. S4(c). While we found the lowest IR-active mode in the tetragonal cell at 2 THz, this frequency is out-of-range of resonant condition with a 0.5 THz field pulse. These results indicate that the FES mode can only be excited by the 0.5 THz field pulse.

A previous study evaluated the frequency of the FES mode from the eigenvalue difference between ground and the first excited states in quantum paraelectric $SrTiO_3$ [13]. We evaluate the IR spectra by solving the time-dependent Schrödinger equation with initial kicking at 2 ps. As shown in Fig. S5, the single peak at $\sim$ 0.47 THz is visible in the spectrum over a

wide range of frequencies. This result indicates that the 2D potential energy surface provides a frequency of FES mode that is consistent with previous experimental observations [21–24].

MODIFIED FREQUENCY OF FES MODE BY ELONGATED LATTICE

The light-induced elongation of the lattice is not enough to lead to the ferroelectric transition in $SrTiO_3$. Indeed a much larger lattice elongation would be required to induce ferroelectricity directly. For example, the THz pulse with $E = 450$ kV/cm leads to ferroelectricity showing $Q_c = 0.04$ Å at 8 ps as shown in Fig. 2(a) of the main text. To prove this behavior, we evaluated the frequency of the FES mode as a function of strain in the quantum paraelectric $SrTiO_3$ as shown in Fig. S6. The static lattice Schrödinger equation is solved with additional strain terms ($H' = -\eta Q_c$). The result indicates that a significant elongation $Q_c \sim 0.1$ Å is required for the ferroelectric transition, which is characterized by the complete softening of the FES frequency ($\omega \to 0$) [25].

EFFECT OF SHAPE OF THZ PULSE ON THE THZ-INDUCED FERROELECTRICITY IN $SRTIO_3$

Our simulation found that the light-mixed state between ground and first excited states of quantum paraelectric $SrTiO_3$ generated by asymmetric single-cycle THz pulses is a viable route for THz field-induced ferroelectricity. We further investigated the control of the THz field-induced ferroelectric phase transition using the THz pulse duration as a tuning knob, as shown in Fig. S7. We applied a THz field pulse, parameterized as follows; $E(t) = E_0 cos(2\pi\omega t) exp(-0.5(t - t_0)^2/\sigma^2)$. We observe that a negatively polarized ferroelectric ($Q_f > 0$) state with a pulse of $E = 130$ kV/cm and $\sigma = 0.7$ ps (see Fig. S7(a)), similar to the main text. On the other hand, a pulse characterized by $E = 160$ kV/cm and $\sigma = 2.0$ ps leads to a positively polarized ferroelectric state ($Q_f > 0$) as shown in Fig S7(b). This behavior indicates that the direction of the electric polarization is a direct consequence of the pulse shape. In particular, as apparent from Fig. S7(b), the FES mode follows the pulse shape and gets trapped in a polarized after a peak in intensity of the laser pulse, which is strong enough to induce ferroelectricity without the inversion symmetry. Because the longer pulse has a narrower bandwidth favoring a resonant coupling with the FES mode as

shown in Fig. S7(d), we find that the longer pulse can lead to a ferroelectric transition with lower field strengths ($E < 100$ kV/cm). It reinforces our interpretation of the field-induced ferroelectricity due to the excitation between ground and first excited states instead of an in-coherency of a shifted wave packet.

We investigated the effect of a continuous THz field, as shown in Fig. S7(e). The continuous THz pulse with $\omega = 0.5$ THz and $E = 400$ kV/cm is applied with turn-on duration $t_0 = 5$ ps. This continuous THz field induces the oscillation of FES mode around the $Q_f = 0$ and elongated Q_c, but it does not lead to the THz field-induced ferroelectricity, unlike the case of pulse with $\sigma = 2.0$ ps. These results indicate that the THz-induced ferroelectricity in $SrTiO_3$ originates from the excitation between the ground and the first excited states in the quantum paraelectric phase and applying the asymmetric single-cycle THz pulse. In addition, we employed the single-cycle pulse with a different frequency, as shown in Fig. S7(f). For the single-cycle pulse with 1 and 0.8 THz, the wavepacket with $\sigma = 0.35$ ps and $\sigma = 0.44$ ps are considered. With this condition, the frequency spectrum of a single cycle shows the same averaged value at $\omega = 0$ THz, as shown in Fig. S7(g). We introduce the frequency-dependent behavior in the main text. It reveals that a resonant condition for the excitation between ground and first excited lattice states is vital for the THz field-induced ferroelectricity in $SrTiO_3$.

EFFECT OF FINITE TEMPERATURE ON THZ FIELD-INDUCED FERROELECTRICITY

Here we investigate the finite temperature effect on the dynamics features in the $SrTiO_3$. We consider two main effects of finite temperature on the FES mode in $SrTiO_3$. The first effect is thermally excited other modes such as AFD mode and a-axis. The second effect is the thermal excitation of FES lattice wavefunction, as shown in Fig. 2(b) of the main manuscript. To investigate these finite temperature effects, at first, we proceeded with AIMD simulations with LDA functional at the given temperature under the thermostat [13]. The averaged values of AFD mode (Q_{AFD}) and in-plane lattice displacements (Q_a) at a given temperature are achieved from the AIMD simulations as shown in Fig. S8(a) and S8(b). We found that the higher temperature leads to the decrement of the average angle of AFD modes toward the $AFD = 0^\circ$ and the expansion of a-axis lattice $Q_a > 0$. This tendency indicates that the

thermally excited AFD mode and in-plane lattice can affect the THz-induced ferroelectricity at high temperatures. To investigate the thermal effect on the frequency of FES mode, we evaluated a 2D potential energy surface consisting of FES and out-plane lattice with lattice distortions along with the AFD and in-plane lattice at a given temperature. We evaluated the frequency of FES mode with and without thermal lattice effect from thermal density matrix as our previous study [13]. As shown in Fig. S8(c), the frequency of FES becomes stiffened with the higher temperature, and the thermal effect of other modes is not significant compared with the case of equilibrium lattice of AFD and a-axis [13]. With these two thermal effects, the increment of FES frequency at the higher temperature leads to the non-resonant condition with THz-field pulse, which degrades the absorption of energy from the pulse. Therefore, this modified frequency by thermal effect prevents the THz-field pulse induced ferroelectricity. This result is consistent with the former experiment that shows degraded TFISH signal and stiffening of FES frequency with high-temperature conditions [21].

EFFECT OF OTHER VIBRATIONAL MODES ACTIVATED BY HIGHLY EXCITED FES MODE THROUGH THE NONLINEAR PHONON INTERACTION

The high intensity of THz pulse can excite various phonon modes through the nonlinear phonon interaction with FES mode, but their feedback on FES mode is not significant. Here, we investigate the excitation of AFD mode and in-plane lattice variation, leading to the nonlinear phonon interaction with FES mode [26]. First, we evaluated how much FES mode is excited by given THz-field pulse using lattice Schrödinger equation with classical AFD mode. The dynamics of the AFD mode is evaluated in length unit (Å), and it can be converted into the rotation angle of the oxygen octahedron ($AFD(^\circ)$) from its cubic geometry. The AFD displacement ($Q_a(^\circ)$) is defined as the angle variation ($Q_a = AFD - AFD^0$) from ground state geometry of tetragonal cell (AFD^0). Without dissipation, we applied the THz field-pulse (400 kV/cm) through the time-propagation with 2D+1D Hamiltonian and evaluated the dynamics that provides maximally $|Q_f| = 0.05$ Å , $Q_c = 0.07$ Å and $Q_a = 0.3^\circ$ at $t > 6$ fs as shown in Figs. S9(a)and S9(b). This result indicates that the THz field pulse can induce the AFD mode through the nonlinear phonon interaction with the FES mode. Second, we proceeded with the *ab initio* molecular dynamics simulation (AIMD) simulation without temperature control to evaluate the dynamics of the a-axis. Mainly, we employed a

$2 \times 2 \times 2$ tetragonal unit cell with an initially displaced atomic position toward the eigenvector of FES mode ($Q_f = 0.05$ Å). For the AIMD simulation, we chose the LDA functional to start the dynamics with paraelectric ground geometry of bulk $SrTiO_3$ [13]. In contrast, PBE functional can misleads the dynamics with the nonlinear phonon interaction in the classical limit by presenting the ferroelectric ground geometry with $|Q_f^{ground}| = 0.075$ Å [13, 27]. We found that the initially displaced FES mode gives an oscillation of in-plane lattice with the amplitude of $Q_{a-axis} = 2$ mÅ as shown in Fig. S9(c). This result also indicates that the THz field pulse can excite the oscillation of in-plane lattice through the nonlinear phonon interaction with FES mode.

To understand the feedback effect on FES mode from these displacements of lattices through the excited FES mode, we evaluate the modified potential energy surface of FES mode with each distortion. As shown in Fig. S9(d), the potential energy surfaces of FES mode are compared with various lattice distortions evaluated from the dynamics. We found that the out-plane lattice (Q_c) largely modifies the potential energy surface of FES, while AFD mode (Q_a) and in-plane lattice (Q_{a-axis}) affect almost negligible. In addition, we evaluate the frequency of FES mode by solving the 2D Schrödinger equation with 2D potential energy surface under the lattice distortions of AFD and a-axis. As shown in Figs. S9(e) and S9(f), the frequency of FES mode has a dependency on the AFD distortion in the wide range, while it does not have significant dependence on the a-axis change in the evaluated range from AIMD. Because of the maximally excited lattice distortions ($|Q_a| < 0.3°$ and $|Q_a| < 3$ mÅ) by FES mode, however, the modification of frequency of FES mode is negligible, as we already verified from the potential energy surface of FES mode. These results indicate that the feedback effect of other modes, which are excited through the nonlinear phonon interaction, is not significant as out-plane and the 2D potential between FES and out-plane lattice is enough to describe the THz-induced dynamics and nonlinear phonon interaction in the bulk $SrTiO_3$.

NONLINEAR PHONON INTERACTION WITH FINITE WAVEVECTOR MODES

Our study mainly considered the anharmonic coupling between gamma FES mode and lattice elongation. Because the FES mode at gamma point is the only infrared-active mode that can be excited by 0.5 THz pulse, our minimal model is considered the FES mode and

its nonlinear interaction with out-plane lattice. Notably, the IR gamma mode can be directly excited by resonant E-field under the dipole approximation, as shown in Fig. S10. To investigate the nonlinear phonon interaction of finite wavenumber mode, here we proceeded with the AIMD simulation from paraelectric geometry (Q_{FES}=0) in the $2 \times 2 \times 2$ supercell without a thermostat. Similar to the previous AIMD simulation, we considered LDA functional to avoid the overestimated dynamics by ferroelectric ground geometry [13]. Considering the THz-pulse excites the IR-active mode at $q = 0$, the FES modes with finite wavevector ($q \neq 0$), which is not IR-active, could be excited through the phonon-phonon scattering such as the interaction between $Q_{FES,q=0}$ and $Q_{FES,q\neq0}$, or Q_c and $Q_{FES,q\neq0}$. We prepared the initially elongated out-plane lattice ($Q_{c-axis} = 0.20$ Å) to excite various phonon modes through nonlinear phonon interaction. Notably, we employed the enormous value of initial elongation to excite the $Q_x^2 Q_c$-type interaction, while the THz-induced out-plane lattice elongation is $Q_{c-axis} \sim 0.05$ Å with 400 kV/cm as shown in Fig. S9(a). As shown in Fig. S10, the initially elongated c-axis induces the other phonon modes and a-axis oscillation. Highly elongated c-axis, a-axis, and gamma AFD modes oriented xy, yz, and zx planes are excited by nonlinear phonon interaction and oscillate during the dynamics as shown in Fig. S10(b) and S10(c). In addition, we investigate the excitation of gamma and $q = 0.5\frac{2\pi}{a_0}$ FES modes, which have π phase difference along the given direction as shown in Fig S10(d). The gamma FES modes oriented along x, y, and z-direction are excited with the maximum magnitude of $|Q_{FES}| = 0.01$ Å as shown in Fig. S10(e). On the other hand, there is negligible excitation of FES modes with finite wavevector ($q = 0.5\frac{2\pi}{a_0}$) along with all three directions, as shown in the upper panel of Fig. S10(f). We also investigate the nonlinear phonon interaction between gamma and $q = 0.5\frac{2\pi}{a_0}$ FES modes. From the previously presented dynamics, as shown in Fig. S9, we evaluated the dynamics of $q = 0.5\frac{2\pi}{a_0}$ FES mode induced by initially excited FES mode as shown in Fig. S10(f) below. It shows that the nonlinear phonon interaction between $q = 0$ and $q = 0.5\frac{2\pi}{a_0}$ FES modes is also negligible, considering the FES modes at gamma are also highly excited($|Q_{FES}| = 0.01$ AA) in this dynamics. These results indicate that nonlinear phonon interaction with finite q-vector can be negligible compared with the interaction between gamma FES mode and c-axis on the THz-induced ferroelectricity in $SrTiO_3$, even though we only considered the zone boundary phonons ($q = 0$ and $q = 0.5\frac{2\pi}{a_0}$).

* dshin@gist.ac.kr

† angel.rubio@mpsd.mpg.de

[1] S. Garashchuk, V. Dixit, B. Gu, and J. Mazzuca, J. Chem. Phys. **138**, 054107 (2013).

[2] C.-C. Chou, Ann. Phys. **362**, 57 (2015).

[3] P. S. Riseborough, P. Hanggi, and U. Weiss, Phys. Rev. A **31**, 471 (1985).

[4] J. Shi, E. Baldini, S. Latini, S. A. Sato, Y. Zhang, B. C. Pein, P.-C. Shen, J. Kong, A. Rubio, N. Gedik, and K. A. Nelson, Nano Lett. **20**, 5214 (2020).

[5] B. R. Mollow, Phys. Rev. A **2**, 1477 (1970).

[6] M. Kozina, M. Fechner, P. Marsik, T. v. Driel, J. M. Glownia, C. Bernhard, M. Radovic, D. Zhu, S. Bonetti, U. Staub, and M. C. Hoffmann, Nat. Phys. **15**, 387 (2019).

[7] P. Ghosez, J.-P. Michenaud, and X. Gonze, Phys. Rev. B **58**, 6224 (1998).

[8] S. H. Shah, P. D. Bristowe, A. M. Kolpak, and A. M. Rappe, Journal of Materials Science **43**, 3750 (2008).

[9] I. Souza, J. Íñiguez, and D. Vanderbilt, Phys. Rev. B **69**, 085106 (2004).

[10] K. Yabana, T. Sugiyama, Y. Shinohara, T. Otobe, and G. F. Bertsch, Phys. Rev. B **85**, 045134 (2011).

[11] P. K. Gogoi and D. Schmidt, Phys. Rev. B **93**, 075204 (2016).

[12] S.-D. Guo and B.-G. Liu, J. Appl. Phys. **110**, 073525 (2011).

[13] D. Shin, S. Latini, C. Schäfer, S. A. Sato, U. De Giovannini, H. Hübener, and A. Rubio, Phys. Rev. B **104**, L060103 (2021).

[14] A. Subedi, A. Cavalleri, and A. Georges, Phys. Rev. B **89**, 220301 (2014).

[15] A. Subedi, Phys. Rev. B **92**, 214303 (2015).

[16] D. M. Juraschek and S. F. Maehrlein, Phys. Rev. B **97**, 174302 (2018).

[17] R. Mankowsky, A. v. Hoegen, M. Först, and A. Cavalleri, Phys. Rev. Lett. **118**, 197601 (2017).

[18] T. F. Nova, A. S. Disa, M. Fechner, and A. Cavalleri, Science **364**, 1075 (2019).

[19] V. A. Abalmasov, Phys. Rev. B **101**, 014102 (2020).

[20] N. Tancogne-Dejean, M. J. T. Oliveira, X. Andrade, H. Appel, C. H. Borca, G. L. Breton, F. Buchholz, A. Castro, S. Corni, A. A. Correa, U. D. Giovannini, A. Delgado, F. G. Eich, J. Flick, G. Gil, A. Gomez, N. Helbig, H. Hübener, R. Jestädt, J. Jornet-Somoza, A. H.

Larsen, I. V. Lebedeva, M. Lüders, M. A. L. Marques, S. T. Ohlmann, S. Pipolo, M. Rampp, C. A. Rozzi, D. A. Strubbe, S. A. Sato, C. Schäfer, I. Theophilou, A. Welden, and A. Rubio, J. Chem. Phys. **152**, 124119 (2020).

[21] X. Li, T. Qiu, J. Zhang, E. Baldini, J. Lu, A. M. Rappe, and K. A. Nelson, Science **364**, 1079 (2019).

[22] G. Shirane and Y. Yamada, Phys. Rev. **177**, 858 (1969).

[23] A. Yamanaka, M. Kataoka, Y. Inaba, K. Inoue, B. Hehlen, and E. Courtens, Europhys. Lett. **50**, 688 (2000).

[24] H. Vogt, Phys. Rev. B **51**, 8046 (1995).

[25] S. Latini, D. Shin, S. A. Sato, C. Schäfer, U. De Giovannini, H. Hübener, and A. Rubio, Proc. Natl. Acad. Sci. USA **118**, e2105618118 (2021).

[26] U. Aschauer and N. A. Spaldin, J. Phys. Condens. Matter **26**, 122203 (2014).

[27] J. C. Wojdel, P. Hermet, M. P. Ljungberg, P. Ghosez, and J. Iniguez, Journal of Physics: Condensed Matter **25**, 305401 (2013).

TABLE S1. Coefficients of 2D potential energy surface with PBE functional for $Q_f = 24$ to $Q_f = 14$ and Q_c

Ry/Å^n	Q_f^{24}	Q_f^{22}	Q_f^{20}	Q_f^{18}	Q_f^{16}	Q_f^{14}
Q_c^0	2.9×10^6	-6.8×10^6	7.1×10^6	-4.3×10^6	1.6×10^6	-4.5×10^5
Q_c^1	-1.4×10^7	3.1×10^7	-2.9×10^7	1.6×10^7	-5.6×10^6	1.3×10^6
Q_c^2	4.6×10^7	-8.9×10^7	7.5×10^7	-3.6×10^7	1.1×10^7	-2.2×10^6
Q_c^3	-1.3×10^8	2.2×10^8	-1.7×10^8	7.1×10^7	-1.8×10^7	3.0×10^6
Q_c^4	1.6×10^8	-2.4×10^8	1.5×10^8	-5.1×10^7	9.4×10^6	-1.0×10^6
Q_c^5	1.2×10^8	-3.0×10^8	2.7×10^8	-1.3×10^8	3.9×10^7	-7.0×10^6
Q_c^6	-2.6×10^8	4.6×10^8	-3.5×10^8	1.4×10^8	-3.4×10^7	4.9×10^6
Q_c^7	-4.1×10^8	8.3×10^8	-6.9×10^8	3.1×10^8	-8.7×10^7	1.5×10^7
Q_c^8	6.8×10^8	-1.2×10^9	8.7×10^8	-3.6×10^8	9.2×10^7	-1.5×10^7
Q_c^9	6.4×10^7	-2.9×10^8	3.1×10^8	-1.6×10^8	5.0×10^7	-9.3×10^6
Q_c^{10}	-2.7×10^8	5.7×10^8	-4.8×10^8	2.2×10^8	-5.9×10^7	9.9×10^6

TABLE S2. Coefficients of 2D potential energy surface with PBE functional for $Q_f = 12$ to $Q_f = 0$ and Q_c

Ry/Å^n	Q_f^{12}	Q_f^{10}	Q_f^8	Q_f^6	Q_f^4	Q_f^2	Q_f^0
Q_c^0	8.7×10^4	-1.2×10^4	1.3×10^3	-1.1×10^2	2.1×10^1	-2.4×10^{-1}	
Q_c^1	-2.1×10^5	2.4×10^4	-2.1×10^3	1.5×10^2	-2.1×10^1	-2.7×10^0	
Q_c^2	2.9×10^5	-2.7×10^4	1.8×10^3	-1.1×10^2	1.1×10^1	2.1×10^0	2.8×10^{-1}
Q_c^3	-3.2×10^5	2.0×10^4	-6.7×10^2	-1.2×10^0	9.4×10^{-1}	-9.5×10^{-1}	-2.1×10^{-1}
Q_c^4	3.5×10^4	4.3×10^3	-6.5×10^2	5.0×10^1	-2.5×10^0	$2/2 \times 10^{-1}$	4.1×10^{-1}
Q_c^5	7.6×10^5	-4.6×10^4	1.2×10^3	3.3×10^1	-4.4×10^0	1.6×10^{-1}	1.1×10^{-1}
Q_c^6	-3.9×10^5	1.1×10^4	7.8×10^2	-8.7×10^1	3.7×10^0	-5.7×10^{-2}	4.1×10^{-1}
Q_c^7	-1.7×10^6	1.1×10^5	-3.7×10^3	8.7×10^0	4.9×10^0	-1.9×10^{-1}	-3.7×10^{-1}
Q_c^8	1.4×10^6	-7.6×10^4	1.3×10^3	8.4×10^1	-5.7×10^0	1.2×10^{-1}	-8.0×10^{-1}
Q_c^9	1.1×10^6	-7.4×10^4	2.7×10^3	-2.5×10^1	-2.5×10^0	1.1×10^{-1}	7.4×10^{-1}
Q_c^{10}	-1.0×10^6	6.2×10^4	-1.6×10^3	-3.2×10^1	3.6×10^0	-9.6×10^{-2}	-5.1×10^{-1}

TABLE S3. Coefficients of 2D potential energy surface with PBE functional for $Q_f = 24$ to $Q_f = 14$ and Q_a

Ry/Å^n	Q_f^{24}	Q_f^{22}	Q_f^{20}	Q_f^{18}	Q_f^{16}	Q_f^{14}
Q_a^1	-4.7×10^6	1.1×10^7	-1.1×10^7	6.7×10^6	-2.6×10^6	6.8×10^5
Q_a^2	-1.2×10^7	2.8×10^7	-2.9×10^7	1.7×10^7	-6.6×10^6	1.7×10^6
Q_a^3	4.2×10^7	-1.0×10^8	1.0×10^8	-6.4×10^7	2.6×10^7	-7.1×10^6
Q_a^4	7.6×10^6	-2.0×10^7	2.6×10^7	-2.1×10^7	1.2×10^7	-4.6×10^6
Q_a^5	-7.1×10^8	1.7×10^9	-1.9×10^9	1.2×10^9	-5.1×10^8	1.5×10^8
Q_a^6	-1.9×10^9	4.7×10^9	-5.5×10^9	3.8×10^9	-1.7×10^9	5.4×10^8
Q_a^7	7.9×10^9	-1.9×10^{10}	2.0×10^{10}	-1.2×10^{10}	4.9×10^9	-1.3×10^9
Q_a^8	6.0×10^{10}	-1.5×10^{11}	1.6×10^{11}	-1.1×10^{11}	4.5×10^{10}	-1.3×10^{10}
Q_a^9	1.4×10^{11}	-3.3×10^{11}	3.7×10^{11}	-2.4×10^{11}	1.0×10^{11}	-3.1×10^{10}
Q_a^{10}	1.0×10^{11}	-2.6×10^{11}	2.8×10^{11}	-1.8×10^{11}	7.9×10^{10}	-2.3×10^{10}

TABLE S4. Coefficients of 2D potential energy surface with PBE functional for $Q_f = 12$ to $Q_f = 0$ and Q_c

Ry/Å^n	Q_f^{12}	Q_f^{10}	Q_f^8	Q_f^6	Q_f^4	Q_f^2	Q_f^0
Q_a^1	-1.2×10^5	1.6×10^4	-1.4×10^3	8.8×10^1	-3.6×10^0	-6.9×10^{-1}	-4.0×10^{-4}
Q_a^2	-3.2×10^5	4.1×10^4	-3.8×10^3	2.5×10^2	-1.2×10^1	2.8×10^0	4.6×10^{-1}
Q_a^3	1.4×10^6	-1.8×10^5	1.6×10^4	-9.5×10^2	2.8×10^1	9.8×10^{-1}	3.4×10^0
Q_a^4	1.2×10^6	-2.2×10^5	2.6×10^4	-1.9×10^3	8.0×10^1	-7.6×10^{-2}	4.9×10^0
Q_a^5	-3.0×10^7	4.1×10^6	-3.8×10^5	2.1×10^4	-6.0×10^2	3.5×10^0	-6.0×10^0
Q_a^6	-1.2×10^8	1.8×10^7	-1.8×10^6	1.1×10^5	-3.8×10^3	6.2×10^1	1.4×10^0
Q_a^7	2.4×10^8	-3.1×10^7	2.6×10^6	-1.3×10^5	2.8×10^3	2.1×10^1	2.2×10^1
Q_a^8	2.7×10^9	-3.8×10^8	3.6×10^7	-2.1×10^6	6.3×10^4	-7.9×10^2	-1.8×10^1
Q_a^9	6.3×10^9	-9.1×10^8	8.6×10^7	-5.0×10^6	-1.6×10^5	-2.1×10^3	-9.9×10^1
Q_a^{10}	4.9×10^9	-7.0×10^8	6.6×10^7	-3.9×10^6	1.2×10^5	-1.6×10^3	-7.6×10^1

TABLE S5. Coefficients of 2D potential energy surface with PBE functional for $Q_a = 10$ to $Q_a = 5$ and Q_c

Ry/Å^n	Q_a^{10}	Q_a^9	Q_a^8	Q_a^7	Q_a^6	Q_a^5
Q_c^1	4.7×10^1	6.1×10^1	1.6×10^1	-8.1×10^0	-2.1×10^0	1.5×10^0
Q_c^2	-6.8×10^0	-8.9×10^0	2.7×10^0	6.4×10^0	2.0×10^0	-1.2×10^{-1}
Q_c^3	6.6×10^1	8.6×10^1	5.2×10^1	2.0×10^1	2.4×10^0	-1.1×10^0
Q_c^4	3.2×10^2	4.2×10^2	1.2×10^2	-4.5×10^1	-2.5×10^1	-8.3×10^{-1}
Q_c^5	-3.8×10^2	-4.9×10^2	-2.9×10^2	-1.1×10^2	-1.4×10^1	5.0×10^0
Q_c^6	-1.7×10^3	-2.2×10^3	-7.0×10^2	1.5×10^2	1.1×10^2	5.6×10^0
Q_c^7	1.1×10^3	1.4×10^3	7.8×10^2	2.5×10^2	2.4×10^1	-1.2×10^1
Q_c^8	2.6×10^3	3.4×10^3	1.1×10^3	-2.5×10^2	-1.7×10^2	-8.5×10^0
Q_c^9	-9.5×10^2	-1.2×10^3	-6.6×10^2	-1.8×10^2	-1.3×10^1	9.7×10^0
Q_c^{10}	-1.3×10^3	-1.7×10^3	-4.9×10^2	1.6×10^2	9.5×10^1	3.3×10^0

TABLE S6. Coefficients of 2D potential energy surface with PBE functional for $Q_a = 4$ to $Q_a = 1$ and Q_c

Ry/Å^n	Q_a^4	Q_a^3	Q_a^2	Q_a^1
Q_c^1	-1.2×10^5	1.6×10^4	-1.4×10^3	8.8×10^1
Q_c^2	-3.2×10^5	4.1×10^4	-3.8×10^3	2.5×10^2
Q_c^3	1.4×10^6	-1.8×10^5	1.6×10^4	-9.5×10^2
Q_c^4	1.2×10^6	-2.2×10^5	2.6×10^4	-1.9×10^3
Q_c^5	-3.0×10^7	4.1×10^6	-3.8×10^5	2.1×10^4
Q_c^6	-1.2×10^8	1.8×10^7	-1.8×10^6	1.1×10^5
Q_c^7	2.4×10^8	-3.1×10^7	2.6×10^6	-1.3×10^5
Q_c^8	2.7×10^9	-3.8×10^8	3.6×10^7	-2.1×10^6
Q_c^9	6.3×10^9	-9.1×10^8	8.6×10^7	-5.0×10^6
Q_c^{10}	4.9×10^9	-7.0×10^8	6.6×10^7	-3.9×10^6

TABLE S7. Information for the $SrTiO_3$ in tetragonal cell

	Sr	Ti	O,z	O,xy
Atomic mass M	87.62	47.86	16	16
Born effective charge Z	2.59	7.30	-5.74	-2.08
Normalized eigenvector U	0.053	0.278	-0.283	-0.235
Number of atom in tetragonal unit cell	4	4	4	8

TABLE S8. Coefficients for the relation between second harmonic generation and ferroelectric soft mode (Q_f)

$1/\mathrm{\AA}^n$	Q_f^3	Q_f^2	Q_f
c_i	1.9×10^{-1}	-8.1×10^{-2}	9.2×10^{-3}

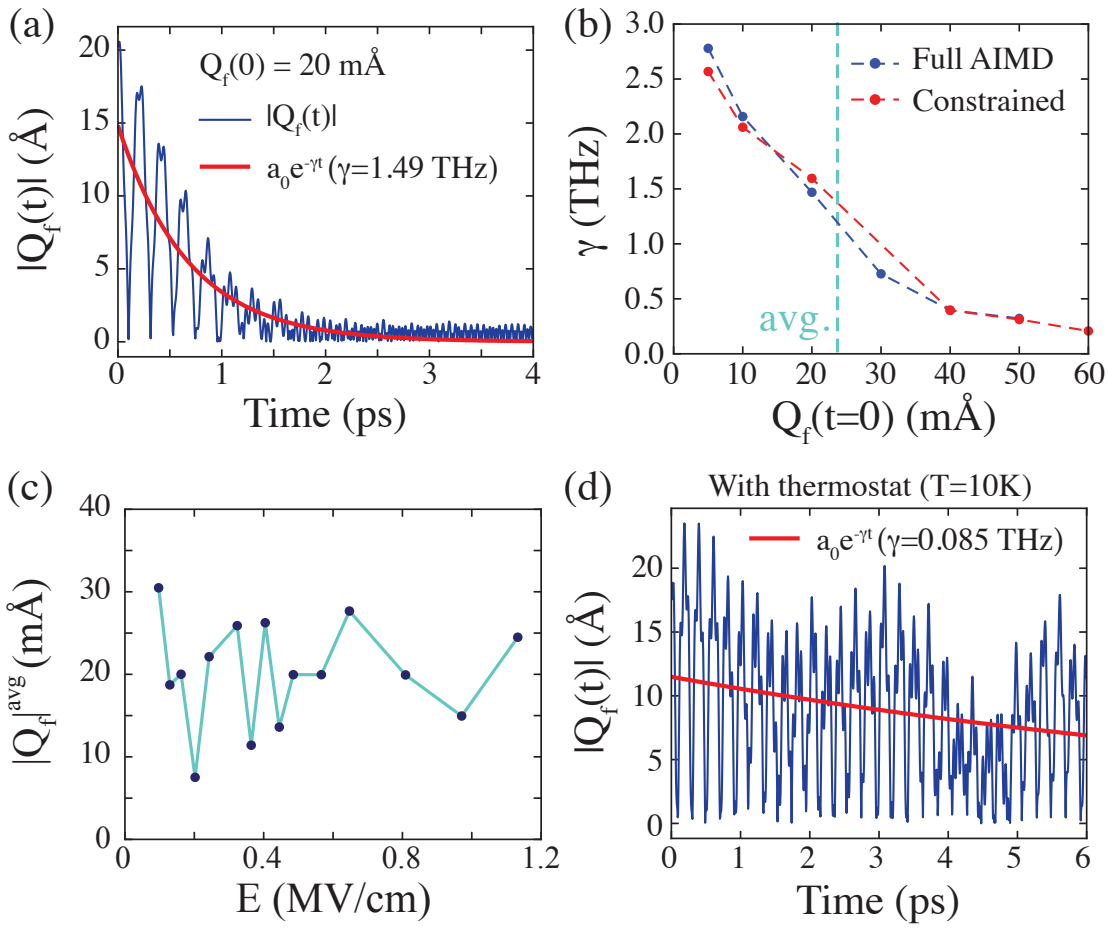

FIG. S1. (a) Time-profile of the absolute value of FES mode with initially displaced atomic geometry along with FES mode ($Q_f(t=0) = 20$ mÅ) and its fitting curve with exponential decay function under NPE-ensemble. (b) Variation of dissipation ratio with given initially displaced FES mode. (c) Averaged absolute value of FES mode induced by THz field pulse without dissipation. (d)Time-profile of the absolute value of FES mode with initially displaced atomic geometry along with FES mode ($Q_f(t=0) = 20$ mÅ) and its fitting curve with exponential decay function under NPT-ensemble.

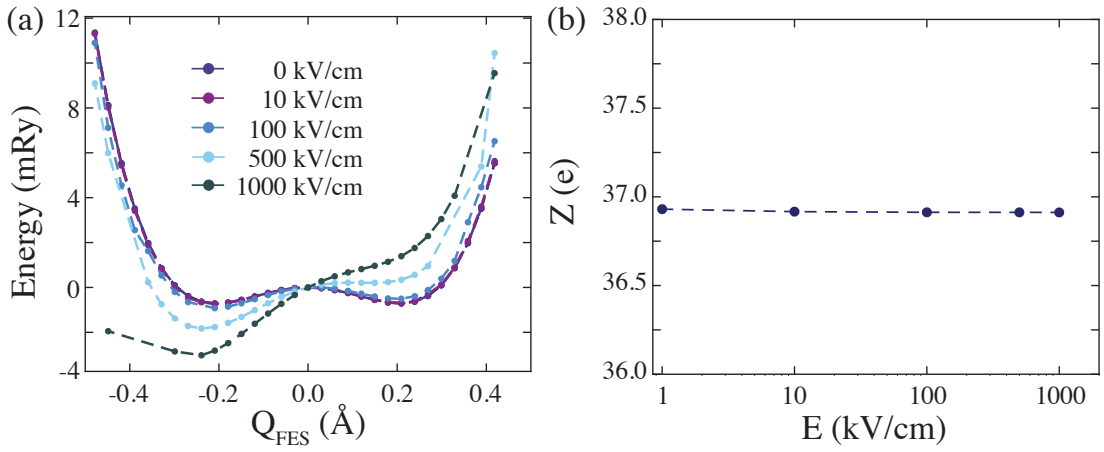

FIG. S2. (a) Modified potential energy surface of FES mode under the given E-field. (b) Mode effective charge evaluated from the modern theory of polarization.

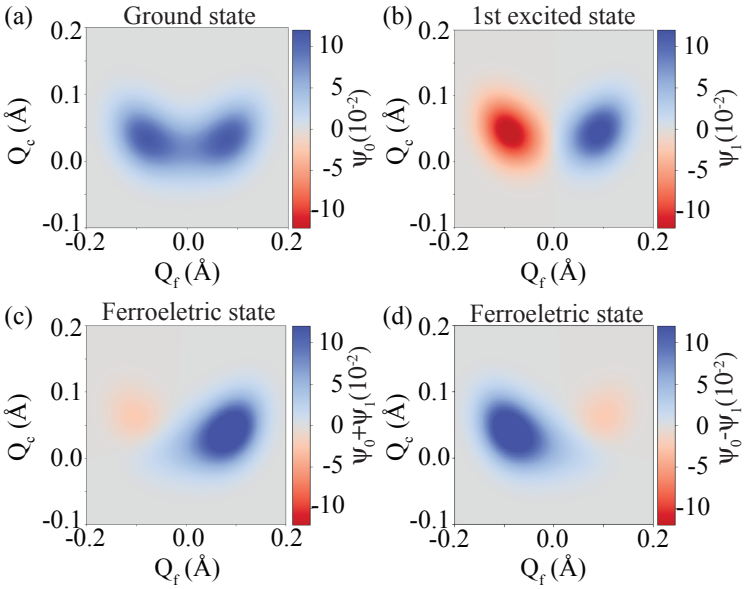

FIG. S3. (a) Ground and (b) first excited states of the quantum paraelectric phase in $SrTiO_3$. The ferroeletric state obtained from linear combination between ground (ψ_0) and first excited (ψ_1) states (c) $\psi_0 + \psi_1$ and (d) $\psi_0 - \psi_1$.

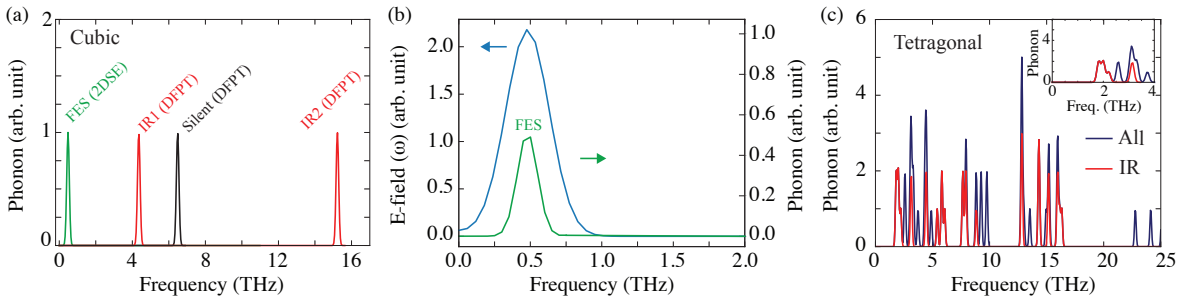

FIG. S4. (a) Phonon density of state in cubic $SrTiO_3$ at $q = 0$. (b) THz-field pulse spectrum in frequency domain (blue) and FES mode (green). (c) Phonon density of state in tetragonal $SrTiO_3$ at $q = 0$. Inset of (c) shows zoomed range between $0 \sim 4$ THz.

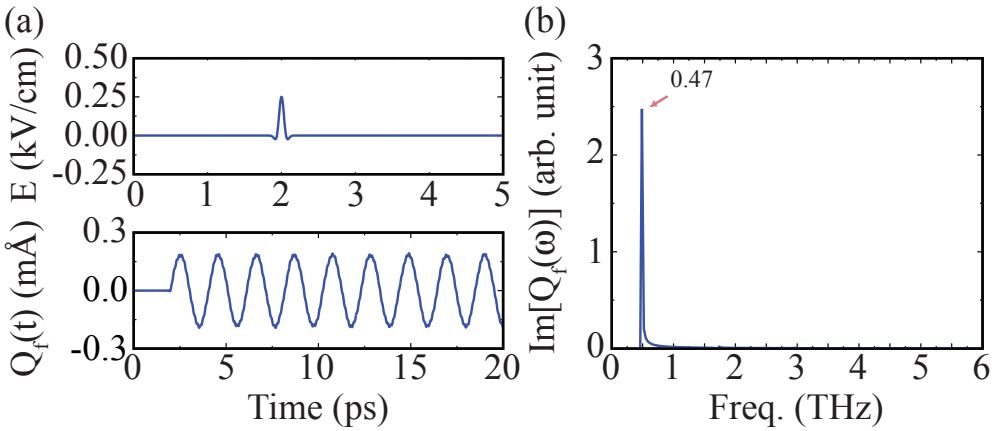

FIG. S5. (a) Time-profile of (upper) applied short E-field pulse and (bottom) expectation value of Q_f. (b) Imaginary part of Fourier component of expectation value of Q_f.

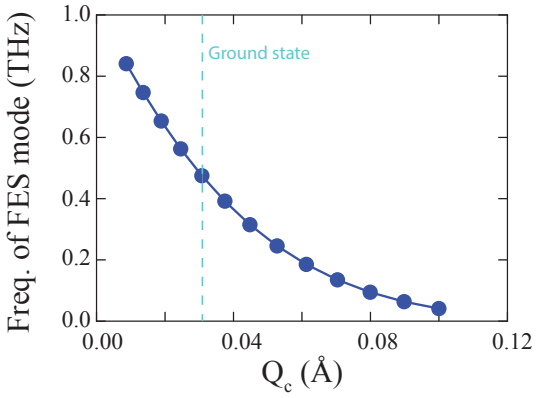

FIG. S6. Frequency of the ferroelectric soft mode as a function of the expectation value of Q_c induced by external strain η. The vertical cyan line indicates the expected value of Q_c in the ground quantum paraelectric state.

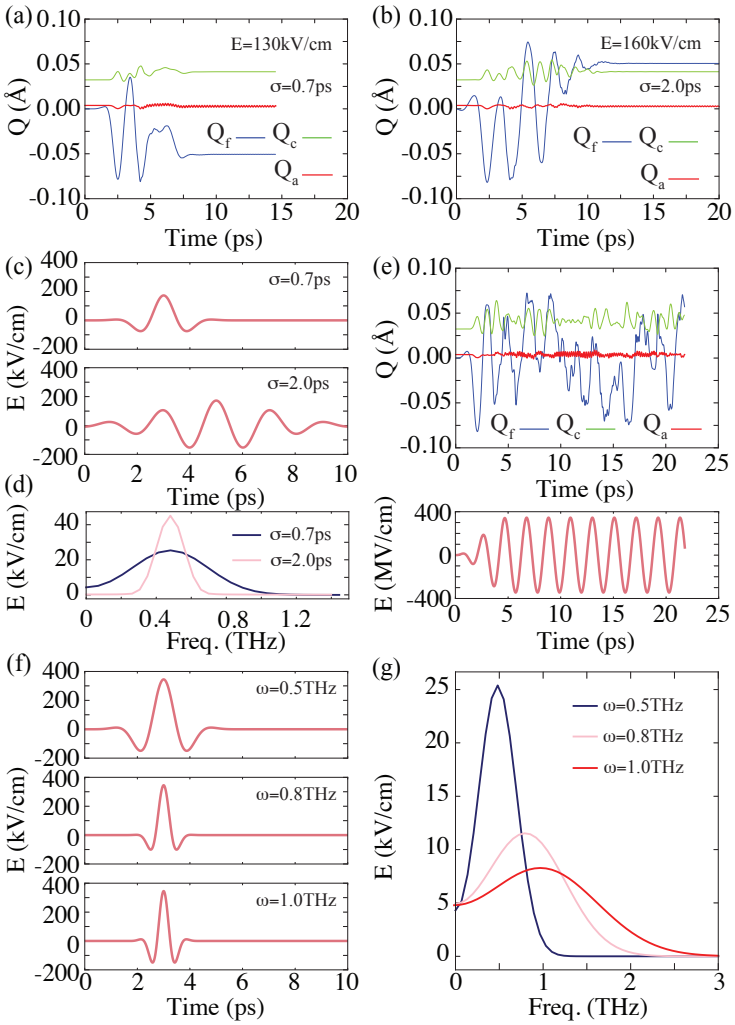

FIG. S7. The effect of THz field pulse shape and frequency. Time-averaged value of FES displacement with different THz field pulse shapes with (a) $E = 130$ kV/cm and $\sigma = 0.7$ ps and (b) $E = 160$ kV/cm and $\sigma = 2.0$ ps. (c) THz field pulse with different gaussian distribution. (d) Spectrum of THz field pulse in frequency domain. (e) Effect of continuous THz field on quantum paraelectric $SrTiO_3$; time-profile of (upper) Q_f and Q_c (bottom) THz pulse. (f) Single cycle THz field pulse with various frequency. (g) Spectrum of single cycle THz field pulse in frequency domain with various frequency.

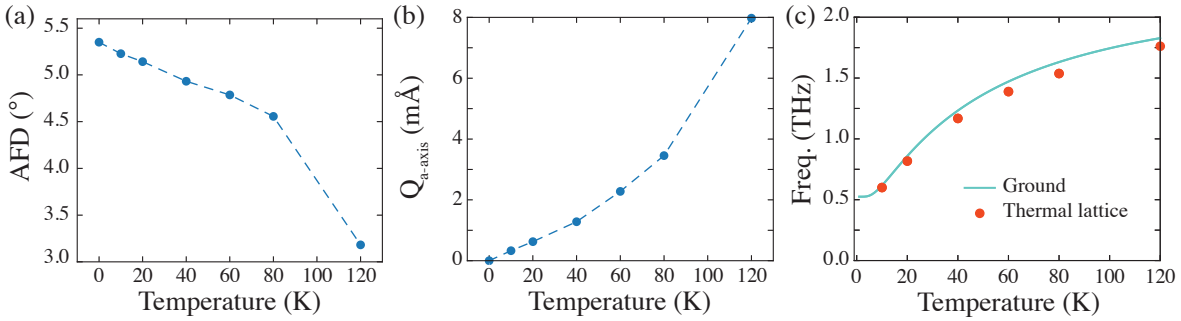

FIG. S8. Temperature-dependent averaged values of (a) AFD angle and (b) a-axis displacement evaluated from AIMD. (c) Temperature dependency of frequency of FES mode modified by excited quantum lattice wavefunction and lattice distortion.

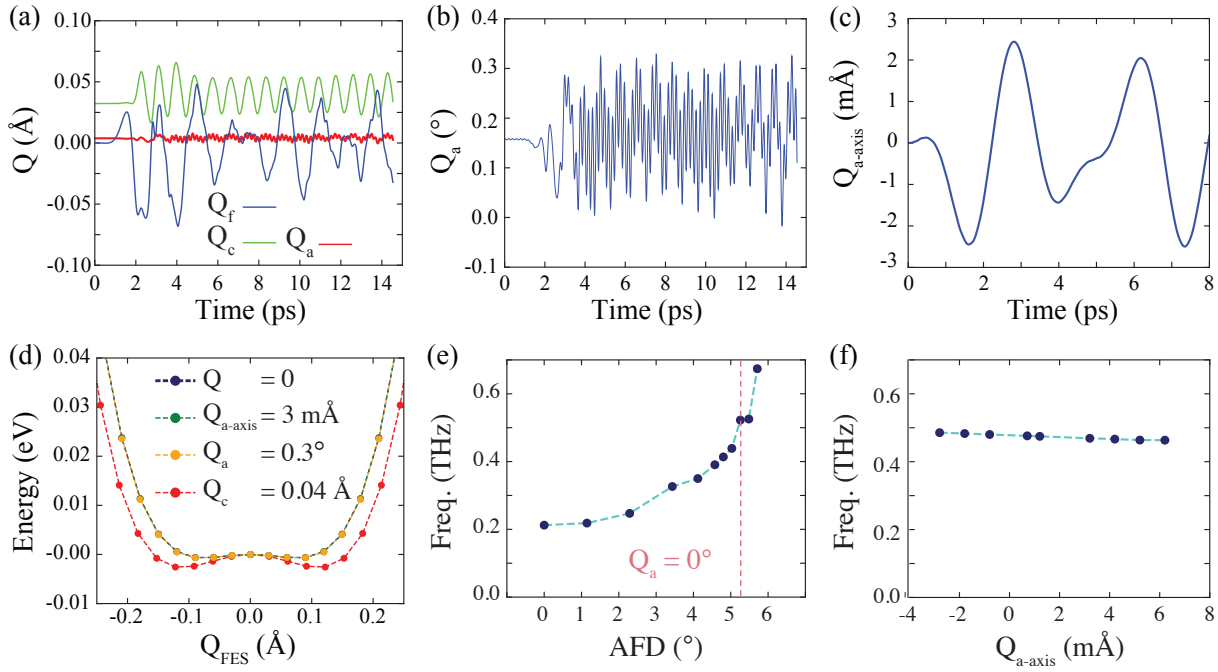

FIG. S9. (a) THz field-induced dynamics of FES mode and c-axis evaluated by 2D Schödinger equation. Time-profile of (b) AFD mode and (c) a-axis induced by initially excited FES mode. (d) Modified potential energy surfaces of FES mode with various lattice distortions. The modified frequency of FES mode by (e) AFD and (f) a-axis displacement, respectively.

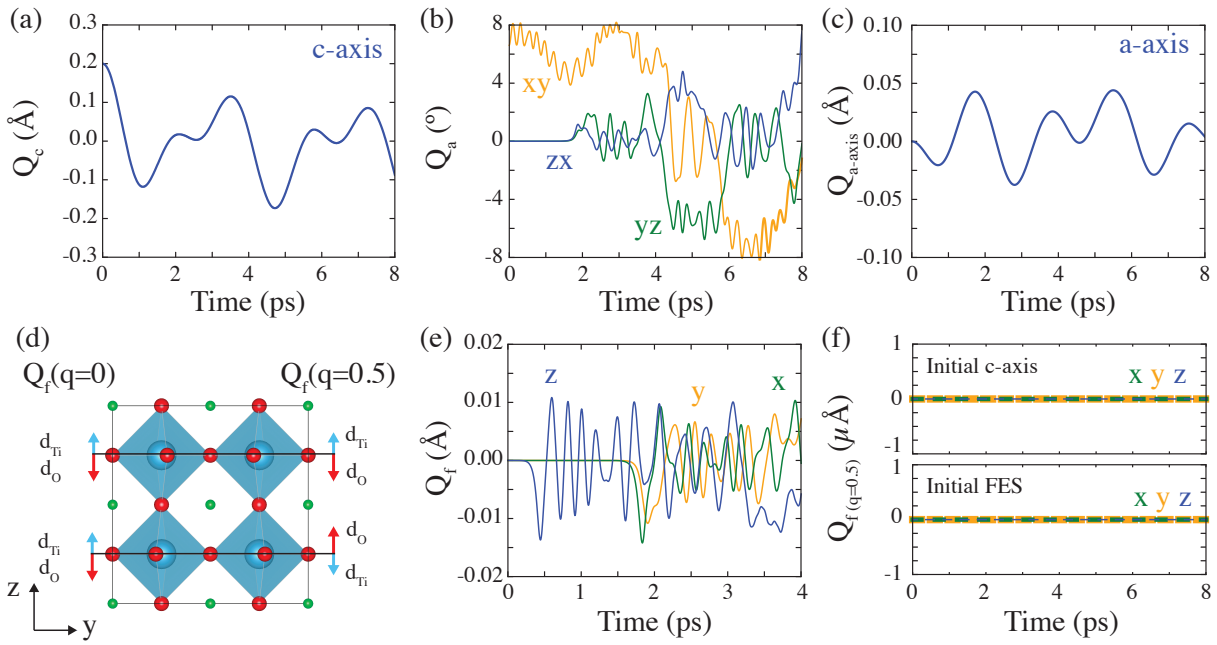

FIG. S10. Time-profile of (a) c-axis, (b) AFD, and (c) a-axis induced by initially elongated c-axis. (d) Schematic image of $Q_{\mathrm{FES}}(q=0)$ and $Q_{\mathrm{FES}}(q=0.5)$. (e) Time-profile of gamma FES modes oriented along x, y, z, direction induced by initially elongated c-axis. (f) Time-profile of $q=0.5\frac{2\pi}{a_0}$ FES modes oriented along x, y, z, direction induced by (upper) initially elongated c-axis and (below) initially excited FES mode.